Model Predictive Control based on Optimized Pulse Patterns for Modular Multilevel Converter STATCOM

Vedrana Spudić, *Member, IEEE* and Tobias Geyer, *Senior Member, IEEE*

Abstract—This paper considers a medium-voltage static synchronous compensator (STATCOM) that is based on a delta-connected modular multilevel converter (MMC) and operates at switching frequencies of 150 Hz or less. Offline computed optimal pulse patterns (OPPs) facilitate the shaping of the grid current spectrum at such low switching frequencies. However, STATCOM applications require the injection of harmonics and negative-sequence currents, as well as fast power transients. In order to achieve this, a model predictive controller is designed, which modifies the switching transitions of the OPPs, inserts additional pulses if required, and controls the circulating current in the delta-connected MMC.

Index Terms—Static synchronous compensator, modular multilevel converter, optimized pulse pattern, model predictive control

I. Introduction

Static synchronous compensators (STATCOMs) are grid-connected power converters that generate or absorb reactive power [1]. Additional objectives include the compensation of harmonics and negative-sequence currents, which result from large dynamic loads, such as arc furnaces. The voltages and currents at the point of common coupling (PCC) with the grid must meet stringent grid codes, which impose limits on the amplitudes of harmonics and inter-harmonics [2].

Modular multilevel converters (MMCs) achieve line-to-line voltages in the medium and high voltage range through the series-connection of unipolar or bipolar modules [3]. This feature makes the MMC topology particularly suitable for grid-connected applications like STATCOMs, as it allows one to reduce or fully eliminate the coupling transformer [4]. Furthermore, due to the large number of voltage levels that can be generated by an MMC, the grid codes can be met with small or even without output filters [5].

The MMC requires a sophisticated control and modulation scheme [6]. Ideally, the controller facilitates the reduction of the filter size while meeting the grid codes, and it allows one to operate the converter at low switching frequencies. This minimizes the losses and enables the use of a simpler and cheaper cooling system. Additional requirements are the control of the circulating current in the delta-connected MMC topology, harmonic injection, a fast dynamic response during transients and the ability to operate under unbalanced grid conditions.

A well-known approach for improving the spectral content of the converter currents is the use of optimal pulse patterns (OPPs) [7]. However, the classic control methodology used with OPP-based modulation, which is described, for example, in [8] and references therein, is not suitable for STATCOM applications, because the application of pre-stored switching angles governed by a slow modulation index selection loop fails to meet the above mentioned control requirements. The literature on OPP-based control methods for STATCOMs is therefore scarce.

Extending [9], an OPP-based model predictive control (MPC) system is proposed in this paper, which provides the benefits of OPP-based modulation, while meeting the control objectives that are required for STATCOMs. A fast online controller, called model predictive pulse pattern control (MP^{3}C), directly modifies the OPP switching instants to achieve fast closed-loop current control. The control method described here extends a related methodology applied to medium-voltage drives, see [10] and subsequent work by the authors for dc-ac MMCs [11] and ac-ac MMC railway interties [12]. To this end, a three-dimensional virtual converter flux at the converter terminals is controlled, such that the desired fundamental and harmonic current components are injected into the PCC. To balance the capacitor voltages of the MMC modules, MP^{3}C needs to also control the circulating current within the MMC.

Classical OPP-based control methods require the switching angles to vary smoothly with the modulation index. Such OPPs are suboptimal with regard to their harmonic performance. This is particularly the case for selective harmonic elimination (SHE) patterns, in which a certain number of harmonic amplitudes are set to zero, see e.g. [13] and [14]. MP^{3}C allows one to drop the smoothness restriction on the switching angles, thus providing additional degrees of freedom to optimize the harmonic spectrum. In particular, OPPs can be designed such that the harmonic content of the voltages and currents is constrained below the amplitude limits prescribed by the grid codes while minimizing the overall distortions.

This paper focuses on delta-connected MMCs for STATCOM applications [15], [16]. The main contribution of this paper is twofold: (i) A high-bandwidth control method is introduced that enables STATCOM operation with OPPs. To the best of the authors' knowledge, such a method has not been previously reported in the literature for STATCOMs. (ii) The benefits of using OPPs for MMC STATCOM are shown, focusing on spectral performance and switching losses.

The authors are with ABB Corporate Research, Baden-Dättwil, Switzerland; e-mail: vedrana.spudic@ch.abb.com, t.geyer@ieee.org
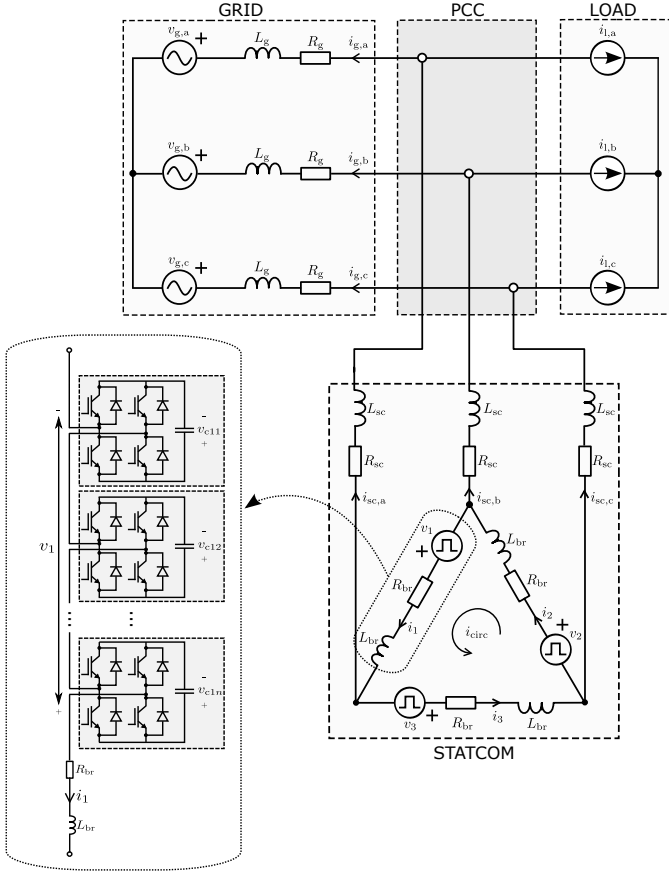
Fig. 1: Delta-connected MMC STATCOM connected to the grid

This result opens up new opportunities for a redesign and optimization of MMC STATCOM systems.

The paper is structured as follows. The STATCOM system is described and modelled in Sect. II, and suitable OPPs are designed in Sect. III. Based on the references derived in Sect. IV, the OPP-based MPC scheme is proposed in Sect. V. Its performance is evaluated in Sect. VI for an industrial case study in several operating conditions. The characteristics of the proposed MPC scheme are discussed in Sect. VII before concluding the paper in Sect. VIII.

II. STATCOM MODELING

As shown in Fig. 1, the delta-connected MMC STATCOM is connected via the PCC to the grid. Other loads connected to the PCC can be considered as a disturbance, which is modeled as the three-phase current source $\boldsymbol{i}_{\mathrm{l,abc}} = [i_{\mathrm{l,a}} \; i_{\mathrm{l,b}} \; i_{\mathrm{l,c}}]^T$[1]. The grid is modeled with an equivalent Thevenin representation, comprising the sinusoidal three-phase voltage source $\boldsymbol{v}_{\mathrm{g,abc}} = [v_{\mathrm{g,a}} \; v_{\mathrm{g,b}} \; v_{\mathrm{g,c}}]^T$, the series inductance L_{g} and the grid resistance R_{g}. We also define the three-phase grid current $\boldsymbol{i}_{\mathrm{g,abc}} = [i_{\mathrm{g,a}} \; i_{\mathrm{g,b}} \; i_{\mathrm{g,c}}]^T$.

---

[1]Throughout this paper, lower-case quantities are variables, lower-case boldface quantities are vectors, upper-case quantities are parameters, and upper-case boldface quantities are matrices.

The delta-connected MMC has three branches. Each branch consists of the series-connection of M bipolar modules, an inductor L_{br} and a (small) resistance R_{br}. The inductance L_{sc} (the subscript sc stands for STATCOM) and resistance R_{sc} model the connection of the MMC to the PCC, see, for example, [17, Chap. 31]. This connection typically includes a transformer.

Each module contains two pairs of switches and a capacitor, see Fig. 1. The voltage of the capacitor is denoted by $v_{\mathrm{c}jk}$, where $j \in \{1, 2, 3\}$ refers to the branch and $k \in \{1, \ldots, M\}$ refers to the module within that branch. By applying different gate signals to the module's switches, the capacitor is either disconnected from the converter branch or it is connected to the converter branch with a positive or negative polarity. The voltage across the module terminals is $v_{jk} = u_{jk}v_{\mathrm{c}jk}$, where $u_{jk} \in \{-1, 0, 1\}$ denotes the switch position, which is the control variable. The voltage of the series-connection of the modules in the jth branch is

$$v_j = \sum_{k=1}^{M} u_{jk}v_{\mathrm{c}jk}. \tag{1}$$

We refer to v_j as the branch voltage, and i_j is correspondingly the branch current. We also define the vectors $\boldsymbol{v}_{123} = [v_1 \; v_2 \; v_3]^T$ and $\boldsymbol{i}_{123} = [i_1 \; i_2 \; i_3]^T$ for the branch voltage and the branch current, respectively.

The circuit in Fig. 1 is described by the following equations that arise from Kirchhoff's laws:

$$\boldsymbol{v}_{123} = L_{\mathrm{br}}\frac{\mathrm{d}\boldsymbol{i}_{123}}{\mathrm{d}t} + R_{\mathrm{br}}\boldsymbol{i}_{123} + \boldsymbol{D}_1\boldsymbol{v}_{\mathrm{g,abc}} + \tag{2a}$$

$$+ \boldsymbol{D}_1\left(L_{\mathrm{sc}}\frac{\mathrm{d}\boldsymbol{i}_{\mathrm{sc,abc}}}{\mathrm{d}t} + R_{\mathrm{sc}}\boldsymbol{i}_{\mathrm{sc,abc}} + L_{\mathrm{g}}\frac{\mathrm{d}\boldsymbol{i}_{\mathrm{g,abc}}}{\mathrm{d}t} + R_{\mathrm{g}}\boldsymbol{i}_{\mathrm{g,abc}}\right),$$

$$\boldsymbol{i}_{\mathrm{sc,abc}} = \boldsymbol{D}_2\boldsymbol{i}_{123}, \tag{2b}$$

$$\boldsymbol{i}_{\mathrm{g,abc}} = \boldsymbol{i}_{\mathrm{sc,abc}} - \boldsymbol{i}_{\mathrm{l,abc}}, \tag{2c}$$

where $\boldsymbol{D}_1 = \begin{bmatrix} 1 & -1 & 0 \\ 0 & 1 & -1 \\ -1 & 0 & 1 \end{bmatrix}$ and $\boldsymbol{D}_2 = \begin{bmatrix} 1 & 0 & -1 \\ -1 & 1 & 0 \\ 0 & -1 & 1 \end{bmatrix}$.

The matrix $\boldsymbol{D}_1$ translates three-phase (abc) quantities to branch (123) quantities, whereas $\boldsymbol{D}_2$ translates branch quantities back to the three-phase system. We refer to the three-phase current at the STATCOM terminals as the converter current $\boldsymbol{i}_{\mathrm{sc,abc}}$ (in contrast to the branch current $\boldsymbol{i}_{123}$), see also (2b).

The Clarke transformation matrix

$$\boldsymbol{K} = \frac{2}{3}\begin{bmatrix} 1 & -\frac{1}{2} & -\frac{1}{2} \\ 0 & \frac{\sqrt{3}}{2} & -\frac{\sqrt{3}}{2} \\ \frac{1}{2} & \frac{1}{2} & \frac{1}{2} \end{bmatrix}$$

transforms three-phase (abc) variables and branch (123) variables into the stationary orthogonal $\alpha\beta\gamma$ reference frame. To
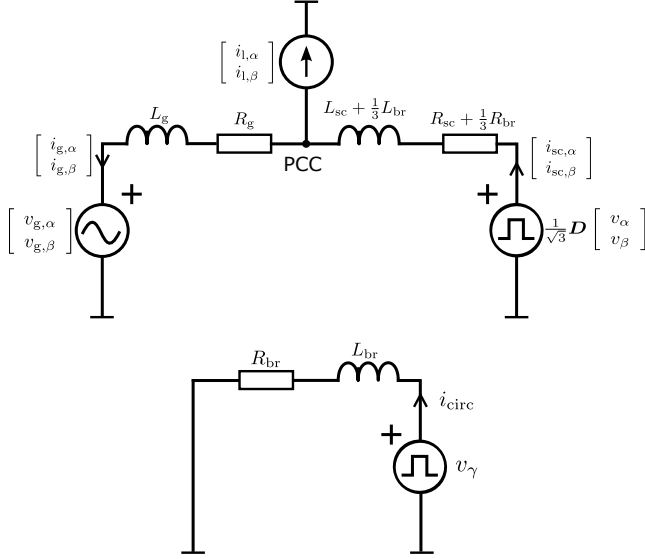
Fig. 2: Equivalent differential-mode and common-mode circuit representations

this end, we introduce the variables

$$\boldsymbol{v}_{\alpha\beta\gamma} = \boldsymbol{K}\boldsymbol{v}_{123},$$
$$\boldsymbol{i}_{\alpha\beta\gamma} = \boldsymbol{K}\boldsymbol{i}_{123},$$
$$\boldsymbol{i}_{\text{sc},\alpha\beta\gamma} = \boldsymbol{K}\boldsymbol{i}_{\text{sc,abc}},$$
$$\boldsymbol{v}_{\text{g},\alpha\beta\gamma} = \boldsymbol{K}\boldsymbol{v}_{\text{g,abc}},$$
$$\boldsymbol{i}_{\text{g},\alpha\beta\gamma} = \boldsymbol{K}\boldsymbol{i}_{\text{g,abc}}.$$

With this, and as shown in Appendix A, (2) can be separated into two sets of equations—one only with differential-mode and the other one only with common-mode components. The differential-mode equations are

$$\frac{1}{\sqrt{3}}\boldsymbol{D}\boldsymbol{v}_{\alpha\beta} = L_{\text{eq}}\frac{\mathrm{d}\boldsymbol{i}_{\text{sc},\alpha\beta}}{\mathrm{d}t} + R_{\text{eq}}\boldsymbol{i}_{\text{sc},\alpha\beta} + \tag{3a}$$

$$+ L_{\text{g}}\frac{\mathrm{d}\boldsymbol{i}_{\text{g},\alpha\beta}}{\mathrm{d}t} + R_{\text{g}}\boldsymbol{i}_{\text{g},\alpha\beta} + \boldsymbol{v}_{\text{g},\alpha\beta},$$

$$\boldsymbol{i}_{\text{g},\alpha\beta} = \boldsymbol{i}_{\text{sc},\alpha\beta} - \boldsymbol{i}_{\text{l},\alpha\beta}, \tag{3b}$$

where $L_{\text{eq}} = L_{\text{sc}} + \frac{1}{3}L_{\text{br}}$ and $R_{\text{eq}} = R_{\text{sc}} + \frac{1}{3}R_{\text{br}}$. The matrix

$$\boldsymbol{D} = \frac{1}{2}\begin{bmatrix} \sqrt{3} & 1 \\ -1 & \sqrt{3} \end{bmatrix} \tag{4}$$

performs a clockwise rotation of a two-dimensional vector by 30°. This rotation arises when translating branch quantities from delta to star configuration. The equations for the differential-mode components describe the currents between the STATCOM $\boldsymbol{i}_{\text{sc},\alpha\beta}$, the grid $\boldsymbol{i}_{\text{g},\alpha\beta}$, and the load $\boldsymbol{i}_{\text{l},\alpha\beta}$. To control the differential-mode converter current $\boldsymbol{i}_{\text{sc},\alpha\beta}$, the differential-mode component of the converter voltage $\boldsymbol{v}_{\alpha\beta}$ can be used, see (3a) and Fig. 2.

Similarly, as shown in Appendix A, the corresponding common-mode equations follow as

$$v_{\gamma} = L_{\text{br}}\frac{\mathrm{d}i_{\text{circ}}}{\mathrm{d}t} + R_{\text{br}}i_{\text{circ}}, \tag{5a}$$

$$i_{\text{g},\gamma} = 0. \tag{5b}$$

The common-mode component of the branch current is non-zero and called the *circulating current*, i.e.

$$i_{\text{circ}} = i_{\gamma} = \frac{1}{3}(i_1 + i_2 + i_3).$$

As can be seen in Fig. 1, the circulating current flows through the converter branches and remains inside the delta-connected converter. Because the circulating current shifts energy between the branches of the converter, it has to be tightly controlled in order to prevent any drift in the module capacitor voltages. To this end, the common-mode component of the converter voltage v_{γ} can be used, see (5a) and Fig. 2. The common-mode component of the grid current $i_{\text{g},\gamma}$ is zero.

III. OPP COMPUTATION

OPPs are computed offline such that the desired spectral properties of the converter current $\boldsymbol{i}_{\text{sc,abc}}$ are achieved. To make this procedure tractable, it is common practise to assume operation at steady state and nominal operating conditions, i.e. the module capacitors are assumed to be constant voltage sources v_{c} and disturbances from the grid are neglected. The expression (1) of the sum of the module voltages in the jth branch then simplifies to

$$v_j = v_{\text{c}}\sum_{k=1}^{M}u_{jk} = v_{\text{c}}u_j,$$

with $j \in \{1, 2, 3\}$, where $u_j \in \{-M, \ldots, 0, \ldots, M\}$ is the branch switch position.

We restrict the OPPs to quarter-wave symmetric pulse patterns, for which $u(\pi - \theta) = u(\theta)$ and $u(\theta + \pi) = -u(\theta)$ hold, where θ is the phase angle. The quarter-wave symmetric pulse pattern is fully characterized by the primary *switching angles* $\theta_1, \ldots, \theta_d$ at which the switching function changes its value, and the primary *switching transitions* $\Delta u_1, \ldots, \Delta u_d$, with $\Delta u_i \in \{-1, 1\}$. For example, $\Delta u_i = 1$ implies that the value of the switching function increases by 1 at the switching angle θ_i.

The integer number d denotes the number of switching transitions of one phase in a quarter of a fundamental period; it is commonly referred to as the *pulse number*. The latter defines the switching frequency of the system. An example of a quarter-wave symmetric pulse pattern with $d = 9$ switching transitions is shown in Fig. 3.

The three-phase pulse pattern over one fundamental period can be constructed from the first quarter-wave of the single-phase pattern by first constructing the single-phase pulse pattern over one 2π-period and the shifting the pulse pattern by $\frac{2\pi}{3}$ and $\frac{4\pi}{3}$ to obtain the pulse patterns in phase b and c, respectively. For more details on OPPs, the reader is referred to [7].

Owing to its 2π-periodicity and quarter-wave symmetry, the OPP can be represented by the Fourier series

$$u(\theta) = \sum_{n=1}^{\infty}\hat{u}_n\sin(n\theta) \tag{6}$$
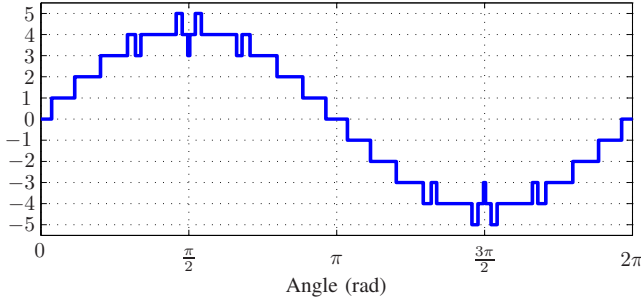
Fig. 3: Quarter-wave symmetric single-phase pulse pattern

with the Fourier coefficient

$$\hat{u}_n = \begin{cases} \dfrac{4}{n\pi} \displaystyle\sum_{i=1}^{d} \Delta u_i \cos(n\alpha_i), & \text{for odd } n, \\[2mm] 0, & \text{for even } n. \end{cases} \quad (7)$$

Quarter-wave symmetric pulse patterns are, by definition, free of even harmonics. Hence the Fourier coefficients $\hat{u}_n$ are zero for even harmonic orders n.

OPPs are computed by solving the following optimization problem for a fixed pulse number d and a given amplitude of the fundamental component $\hat{u}_1$:

$$\min_{\substack{\theta_1,\dots,\theta_d \\ \Delta u_1,\dots,\Delta u_d}} \sum_{\substack{n=2k+1, k\in\mathbb{N} \\ n\leq N}} C_n \left(\frac{1}{n^2} \sum_{i=1}^{d} \Delta u_i \cos(n\theta_i) \right)^2 \quad (8a)$$

$$\text{subj. to } 0 \leq \theta_1 \leq \theta_2 \leq \cdots \leq \theta_d \leq \frac{\pi}{2} \quad (8b)$$

$$\sum_{i=1}^{j} \Delta u_i \leq M, \quad \forall j \in \{1,\dots,d\} \quad (8c)$$

$$\frac{4}{\pi} \sum_{i=1}^{d} \Delta u_i \cos(\theta_i) = \hat{u}_1 \quad (8d)$$

$$\left| \frac{v_c}{k^2 \omega_1 (L_g + L_{eq})\pi} \sum_{i=1}^{d} \Delta u_i \cos(k\theta_i) \right| \leq \hat{i}_{k,\text{lim}}, \forall k \in \mathcal{K}. \quad (8e)$$

The d switching angles θ_i and switching transitions Δu_i constitute the optimization (or decision) variables. The objective function (8a) penalizes the sum of the (weighted) amplitudes of the switching function's harmonic spectrum. Thanks to the quarter-wave symmetry, only odd harmonics need to be considered. We distinguish between differential-mode and common-mode harmonics. For a $\frac{2\pi}{3}$ phase shift between the converter branches, all non-triplen harmonics are differential-mode harmonics, which give rise to converter current harmonics. Triplen harmonics constitute common-mode harmonics, which drive circulating current harmonics, see Sect. II. To account for this difference, triplen and non-triplen harmonics can be penalized differently by choosing the weighting coefficients C_n accordingly. If the coefficients for the non-triplen harmonics are the same and those for the triplen harmonics are zero, the objective function penalizes the

total harmonic distortion (THD) of the converter current, see [18]. The highest harmonic order considered in the objective function is denoted by N.

Constraint (8b) imposes an ascending order on the switching angles. The addition of constraint (8c) ensures that the pulse pattern can be synthesized by an M-level converter. Constraint (8d) ensures that the amplitude of the switching function's fundamental component is equal to $\hat{u}_1$.

Constraint (8e) ensures that the spectral limits imposed by the grid codes are met. Here, v_c denotes again the nominal voltage of the module capacitors, $\omega_1 = 2\pi f_1$ is the angular fundamental frequency and $L_g + L_{eq}$ is the equivalent grid inductance. The relevant grid code defines the limits $\hat{i}_{k,\text{lim}}$. The set $\mathcal{K}$ contains odd non-triplen harmonic orders, typically up to the harmonic order of $N = 180$.

Because the switching transitions are restricted to the set $\{-1, 0, 1\}$, the optimization problem (8) is a mixed-integer nonlinear program. Rather than solving it directly, it can be solved indirectly by enumerating feasible switching sequences. The set of investigated switching sequences can be significantly reduced by employing heuristics, e.g., by eliminating switching sequences that lead to high common-mode voltages that drive undesired circulating currents and increase losses. For a given switching sequence, (8) simplifies to a non-convex but real-valued optimization problem, in which the switching transitions are given and the switching angles are the only optimization variables. Real-valued optimization problems can be solved relatively efficiently, but require multiple different initial conditions owing to their non-convex nature. For more details on formulating and solving OPP optimization problems for multi-level converters, the reader is referred to [19].

To enable the operation of the system at different operating points (corresponding to e.g. different reactive power references), OPPs are computed for a range of fundamental amplitudes $\hat{u}_1$. Moreover, to enable operation at different switching frequencies, the OPPs are typically computed for a range of pulse numbers d. The primary switching angles and primary switching sequences are stored in the controller memory.

IV. MODELING FOR REFERENCE GENERATION

In this section, we derive a slightly simplified model of the STATCOM system, based on which we will generate references for the control loops, see Sects. V-A and V-B. To this end, we adopt the notion of virtual fluxes, which are defined as the time integral of the voltage v

$$\psi(t) = \int_0^t v(\tau)\mathrm{d}\tau.$$

Virtual fluxes generalize flux linkages in electrical machines. In this paper, we use the terms *flux* and *virtual flux* interchangeably.
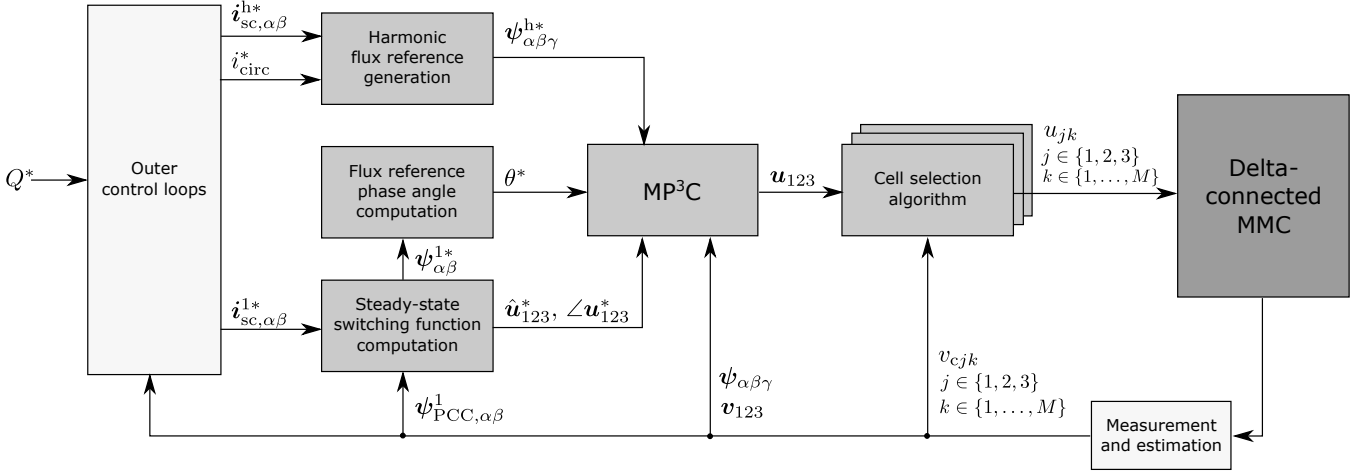
Fig. 4: Block diagram of the OPP-based model predictive control system for the delta-connected MMC STATCOM

We introduce the virtual converter flux and the grid flux

$$\boldsymbol{\psi}_{\alpha\beta} = \int_0^t \boldsymbol{v}_{\alpha\beta}(\tau)\mathrm{d}\tau, \quad \psi_\gamma = \int_0^t v_\gamma(\tau)\mathrm{d}\tau, \quad (9\mathrm{a})$$

$$\boldsymbol{\psi}_{\mathrm{g},\alpha\beta} = \int_0^t \boldsymbol{v}_{\mathrm{g},\alpha\beta}(\tau)\mathrm{d}\tau, \quad (9\mathrm{b})$$

integrate (3a) and (5a), and neglect all ohmic resistances. This leads to the model

$$\frac{1}{\sqrt{3}}\boldsymbol{D}\boldsymbol{\psi}_{\alpha\beta} = L_{\mathrm{eq}}\boldsymbol{i}_{\mathrm{sc},\alpha\beta} + L_{\mathrm{g}}\boldsymbol{i}_{\mathrm{g},\alpha\beta} + \boldsymbol{\psi}_{\mathrm{g},\alpha\beta}, \quad (10\mathrm{a})$$

$$\psi_\gamma = L_{\mathrm{br}}i_{\mathrm{circ}}. \quad (10\mathrm{b})$$

We distinguish between fundamental components, which we denote by the superscript [1], and harmonic components, to which we refer with the superscript [h]. We apply this principle of superposition to the virtual converter flux, converter current, load current and grid current, and define

$$\boldsymbol{\psi}_{\alpha\beta} = \boldsymbol{\psi}_{\alpha\beta}^1 + \boldsymbol{\psi}_{\alpha\beta}^{\mathrm{h}}, \quad (11\mathrm{a})$$

$$\boldsymbol{i}_{\mathrm{sc},\alpha\beta} = \boldsymbol{i}_{\mathrm{sc},\alpha\beta}^1 + \boldsymbol{i}_{\mathrm{sc},\alpha\beta}^{\mathrm{h}}, \quad (11\mathrm{b})$$

$$\boldsymbol{i}_{\mathrm{l},\alpha\beta} = \boldsymbol{i}_{\mathrm{l},\alpha\beta}^1 + \boldsymbol{i}_{\mathrm{l},\alpha\beta}^{\mathrm{h}}, \quad (11\mathrm{c})$$

$$\boldsymbol{i}_{\mathrm{g},\alpha\beta} = \boldsymbol{i}_{\mathrm{g},\alpha\beta}^1 + \boldsymbol{i}_{\mathrm{g},\alpha\beta}^{\mathrm{h}}. \quad (11\mathrm{d})$$

We also define the fundamental component of the virtual flux at the PCC as

$$\boldsymbol{\psi}_{\mathrm{PCC},\alpha\beta}^1 = L_{\mathrm{g}}\boldsymbol{i}_{\mathrm{g},\alpha\beta}^1 + \boldsymbol{\psi}_{\mathrm{g},\alpha\beta}. \quad (12)$$

The grid voltage and the virtual grid flux are, by definition, free of harmonics. Note that the objective of the STATCOM is to remove all significant harmonics from the grid current. We may thus assume that the virtual PCC flux consists only of a fundamental component, which can be easily estimated from the measured voltage at the PCC.

With the definitions (11) and (12), we can separate the model (10) into the fundamental-component model

$$\frac{1}{\sqrt{3}}\boldsymbol{D}\boldsymbol{\psi}_{\alpha\beta}^1 = L_{\mathrm{eq}}\boldsymbol{i}_{\mathrm{sc},\alpha\beta}^1 + \boldsymbol{\psi}_{\mathrm{PCC},\alpha\beta}^1, \quad (13\mathrm{a})$$

$$\psi_\gamma^1 = L_{\mathrm{br}}i_{\mathrm{circ}}^1, \quad (13\mathrm{b})$$

and the harmonic model

$$\frac{1}{\sqrt{3}}\boldsymbol{D}\boldsymbol{\psi}_{\alpha\beta}^{\mathrm{h}} = (L_{\mathrm{g}} + L_{\mathrm{eq}})\boldsymbol{i}_{\mathrm{sc},\alpha\beta}^{\mathrm{h}} - L_{\mathrm{g}}\boldsymbol{i}_{\mathrm{l},\alpha\beta}^{\mathrm{h}}, \quad (14\mathrm{a})$$

$$\psi_\gamma^{\mathrm{h}} = L_{\mathrm{br}}i_{\mathrm{circ}}^{\mathrm{h}}. \quad (14\mathrm{b})$$

Note that we used (3b) when deriving (14a).

V. OPP-BASED MPC

The OPPs computed in Sect. III are modified online to ensure the precise tracking of the virtual converter flux reference, in order to ensure fast responses to power steps, as well as the injection of harmonics and negative-sequence components. These characteristics are achieved by the proposed model predictive control system, whose block diagram is shown in Fig. 4.

A. Outer Control Loops

The outer control loops provide the following three references to the inner control loops. We denote references by the superscript *.

Differential-mode fundamental current reference $\boldsymbol{i}_{\mathrm{sc},\alpha\beta}^{1*}$. This reference is typically obtained from the reactive power setpoint Q^* or from the grid voltage regulation loop. During steady-state operation, $\boldsymbol{i}_{\mathrm{sc},\alpha\beta}^{1*}$ contains only the fundamental component without additional harmonics. In balanced steady-state conditions, $\boldsymbol{i}_{\mathrm{sc},\alpha\beta}^{1*}$ corresponds to two sinusoidal waveforms of the same amplitude that are phase shifted by $\frac{\pi}{2}$. In the case of unbalanced operation, owing, for example, to an asymmetric fault in the grid, the phase shift could differ from $\frac{\pi}{2}$ and the two amplitudes could be different from one another.

Harmonic current reference $\boldsymbol{i}_{\mathrm{sc},\alpha\beta}^{\mathrm{h}*}$. This reference facilitates the compensation of grid or load harmonic components, which are injected, for example, by arc furnaces. The reference contains the time-evolution of higher-order harmonic currents without a fundamental component.

Circulating current reference i_{circ}^*. For symmetric grid conditions, the circulating current reference is typically zero to avoid unnecessary switching and conduction losses. Additional

harmonics might be added to the circulating current reference to achieve operation during unbalanced conditions and to meet additional objectives, such as the minimization of the capacitor voltage ripple [20]. In both cases, energy stored in the module capacitors is shifted between the branches.

B. Reference Generation for MP^{3}C

MP^{3}C regulates the virtual converter flux vector along its reference trajectory. Three computational entities provide the necessary references and inputs to MP^{3}C. These entities are shown on the left-hand side of Fig. 4 and will be explained below.

Steady-state switching function. Given the differential-mode fundamental converter current reference $\boldsymbol{i}^{1*}_{\mathrm{sc},\alpha\beta}$ and the estimated virtual PCC flux vector $\boldsymbol{\psi}^1_{\mathrm{PCC},\alpha\beta}$, the reference for the fundamental component of the virtual converter flux $\boldsymbol{\psi}^{1*}_{\alpha\beta}$ directly follows from (13a). As shown in Appendix B, the corresponding converter voltage reference $\boldsymbol{v}^{1*}_{\alpha\beta}$ follows from (22), based on which the amplitudes $\hat{\boldsymbol{u}}^*_{123}$ and relative phase angles $\angle\boldsymbol{u}^*_{123}$ of the switching functions are computed (assuming nominal capacitor voltages). This is done for each one of the three converter branches. Based on the outputs of this block, appropriate OPPs are loaded and the optimal flux trajectory is defined for steady-state operation.

During steady-state operation, the amplitudes $\hat{\boldsymbol{u}}^*_{123}$ and relative phase angles $\angle\boldsymbol{u}^*_{123}$ are constant. In balanced conditions, the switching functions in the three branches have the same amplitude and a relative phase shift of $\frac{2\pi}{3}$. In unbalanced conditions, however, the amplitudes of the switching functions in the three branches generally differ, as do the phase shifts between them. Such a scenario will be considered in Sect. VI-C and requires the use of three different OPPs—one per phase.

Flux reference phase angle. The reference for the fundamental component of the virtual converter flux $\boldsymbol{\psi}^{1*}_{\alpha\beta}$ was computed in the entity discussed above. Its phase angle follows from $\theta^* = \arctan \psi^{1*}_\beta / \psi^{1*}_\alpha$, which corresponds to the phase angle of the OPP.

Harmonic flux reference. Based on the references for the harmonic converter current $\boldsymbol{i}^{\mathrm{h}*}_{\mathrm{sc},\alpha\beta}$ and the harmonic circulating current $i^{\mathrm{h}*}_{\mathrm{circ}}$, the reference for the virtual harmonic converter flux

$$\boldsymbol{\psi}^{\mathrm{h}*}_{\alpha\beta\gamma} = \begin{bmatrix} \sqrt{3}\boldsymbol{D}^T(L_{\mathrm{g}}+L_{\mathrm{eq}})\boldsymbol{i}^{\mathrm{h}*}_{\mathrm{sc},\alpha\beta} \\ L_{\mathrm{br}}i^{\mathrm{h}*}_{\mathrm{circ}} \end{bmatrix}$$

is derived from (14). To do so, the reference for the harmonic load current $\boldsymbol{i}^{\mathrm{h}*}_{\mathrm{l},\alpha\beta}$ is set to zero, and $\boldsymbol{D}^{-1} = \boldsymbol{D}^T$ is used.

C. MP^{3}C

The MP^{3}C block diagram is shown in Fig. 5. Its three blocks are described hereafter.

OPP selection and flux trajectory. Based on the required fundamental components of the switching functions $\hat{\boldsymbol{u}}^*_{123}$, the OPPs are loaded from memory. Starting from the primary switching angles and transitions, the switching pattern over the fundamental period is unwrapped by exploiting quarter-wave symmetry. To allow for unbalanced operating conditions, three different OPPs are considered, one per converter branch.
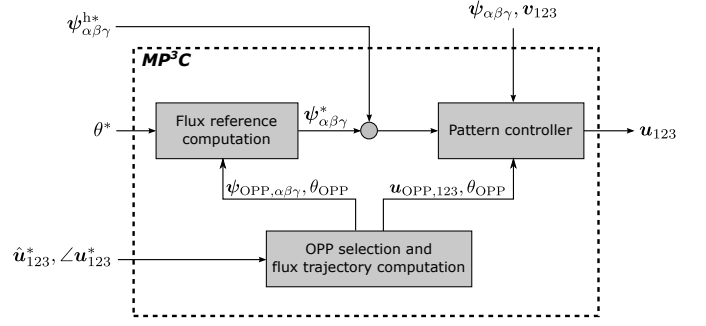
Fig. 5: Block diagram of MP^{3}C

The three single-phase OPPs are combined in one three-phase OPP with the switching function $\boldsymbol{u}_{\mathrm{OPP},123}$ that has switching transitions at the angles θ_{OPP}.

To compute the virtual flux trajectory corresponding to the OPP, the switching functions are multiplied by the nominal module capacitor voltage to obtain the nominal branch voltages. These voltages are transformed into the stationary orthogonal coordinate system and then integrated over time to obtain the virtual flux trajectory $\boldsymbol{\psi}_{\mathrm{OPP},\alpha\beta\gamma}$.

Since the nominal branch voltage is piecewise constant, the resulting virtual flux trajectory is piecewise affine. It thus suffices to compute its corner points, in between which the trajectory can be interpolated. Because the OPPs in the three branches have, in general, different fundamental components with different amplitudes and phase shifts between them, it is advisable to compute the corner points of the virtual flux trajectory online (rather than offline).

Flux reference vector. The flux reference angle θ^* determines the point on the virtual flux reference trajectory that is to be tracked. The exact point on the reference trajectory is obtained by interpolating between its corner points using the information stored in θ_{OPP} and $\boldsymbol{\psi}_{\mathrm{OPP},\alpha\beta\gamma}$.

Pattern controller. The model predictive pattern controller is based on the following principle [10]: A flux error in the jth branch $\Delta\psi_j = \psi^*_j - \psi_j$ can be removed by shifting the ith switching transition in that phase by the time $\Delta t_{ji} = -\frac{\Delta\psi_j}{\Delta u_{ji}v_{\mathrm{c}}}$, where Δu_{ji} is the sign of the ith switching transition and v_{c} is the nominal capacitor voltage. A positive Δt_{ji} implies that the switching transition needs to be postponed, whereas a negative Δt_{ji} means that the switching transition is to be moved forward in time. This simple observation follows directly from the definition of the virtual flux (9a) and the assumption of the branch voltages being piecewise constant waveforms.

In the stationary orthogonal reference frame, the flux error compensation problem can be formulated as the constrained
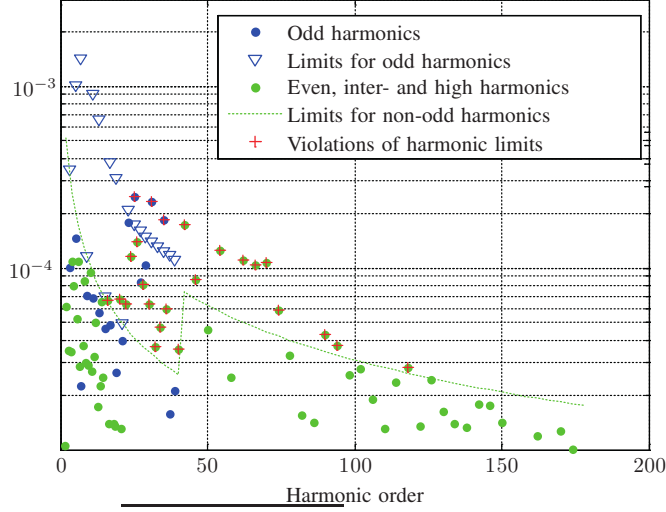
(a) Carrier-based PWM at 150 Hz switching frequency: baseline harmonic spectrum
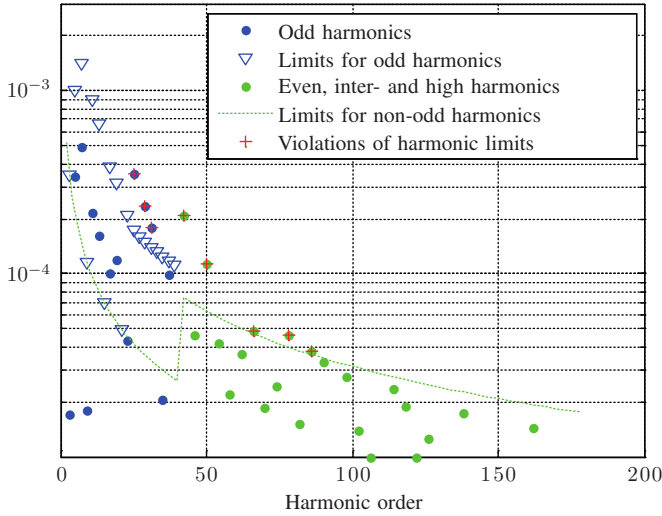
(b) MP³C at 50 Hz switching frequency: slightly improved harmonic spectrum with respect to CB-PWM and 60% lower switching losses
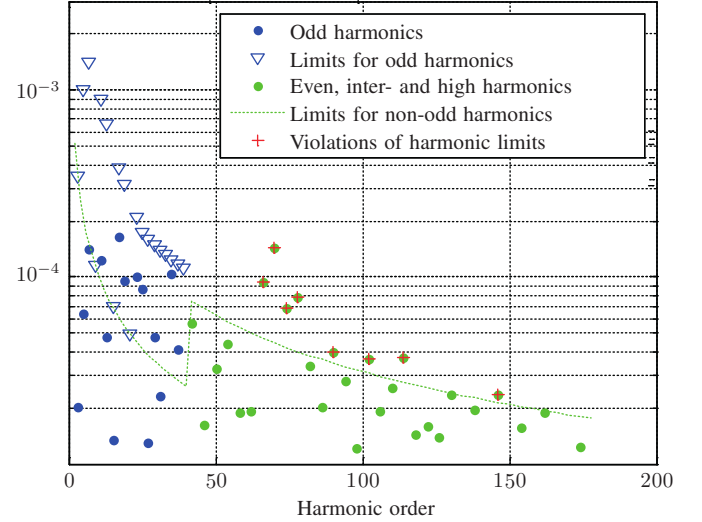
(c) MP³C at 150 Hz switching frequency: similar switching losses as CB-PWM, but with a significantly improved harmonic spectrum

Fig. 6: Harmonic converter current spectrum during steady-state operation at nominal capacitive reactive power

optimization problem

$$\min_{\Delta \boldsymbol{t}} \left\| \boldsymbol{\psi}^*_{\alpha\beta\gamma} - \boldsymbol{\psi}_{\alpha\beta\gamma} - \boldsymbol{\psi}_{\alpha\beta\gamma,\mathrm{corr}}(\Delta \boldsymbol{t}) \right\|_2^2 + \Delta \boldsymbol{t}^T \boldsymbol{Q} \Delta \boldsymbol{t} \quad (15a)$$

$$\text{subj. to } kT_s \leq t_{11} \leq t_{12} \leq \cdots \leq t_{1n_1} \leq t^*_{1(n_1+1)} \quad (15b)$$

$$kT_s \leq t_{21} \leq t_{22} \leq \cdots \leq t_{2n_2} \leq t^*_{2(n_2+1)} \quad (15c)$$

$$kT_s \leq t_{31} \leq t_{32} \leq \cdots \leq t_{3n_3} \leq t^*_{3(n_3+1)}. \quad (15d)$$

The number of OPP switching transitions in the prediction horizon is denoted by n_1, n_2 and n_3 for the three branches. The ith nominal switching instant and the ith switching transition in branch 1 are denoted by t^*_{1i} and Δu^*_{1i}, respectively. The nominal switching instants and switching transitions in branches 2 and 3 are defined accordingly.

The corrections of the switching instants are aggregated in the optimization variable

$$\Delta \boldsymbol{t} = [\Delta t_{11} \ldots \Delta t_{1n_1} \ \Delta t_{21} \ldots \Delta t_{2n_2} \ \Delta t_{31} \ldots \Delta t_{3n_3}]^T.$$

For branch 1, for example, the correction of the ith switching instant is given by $\Delta t_{1i} = t_{1i} - t^*_{1i}$, where t_{1i} denotes the modified ith switching instant.

The virtual flux error is given by $\boldsymbol{\psi}^*_{\alpha\beta\gamma} - \boldsymbol{\psi}_{\alpha\beta\gamma}$, where $\boldsymbol{\psi}_{\alpha\beta\gamma}$ is the estimated virtual converter flux at the terminals of the MMC. The correction of the virtual flux error throughout the prediction horizon is achieved by

$$\boldsymbol{\psi}_{\alpha\beta\gamma,\mathrm{corr}}(\Delta \boldsymbol{t}) = -v_{\mathrm{c}} \boldsymbol{K} \begin{bmatrix} \sum_{i=1}^{n_1} \Delta t_{1i} \Delta u_{1i} \\ \sum_{i=1}^{n_2} \Delta t_{2i} \Delta u_{2i} \\ \sum_{i=1}^{n_3} \Delta t_{3i} \Delta u_{3i} \end{bmatrix}.$$

Note that the flux correction is a linear function in the optimization variable. Its squared two norm, which is denoted

by $||\cdot||_2^2$, is a quadratic function in Δt. The term $\Delta t^T Q \Delta t$ in the objective function (15a) penalizes modifications of the switching instants with the aim to preserve the nominal OPP if possible. The matrix Q is positive definite and diagonal; it sets the trade-off between switching time modifications and controller bandwidth. We set all diagonal entries in Q to the same small value, such as 0.001. The term $\Delta t^T Q \Delta t$ is a quadratic function in Δt.

The constraints (15b)–(15d) ensure that the order of the switching transitions is kept in each branch. That means that each switching transition can be moved forward in time at most until the previous switching instant in the same branch or, in the case of the first upcoming switching instant, to the current time step kT_s. Switching transitions can be delayed at most until the next switching transition in the same branch or, in the case of the last switching transition considered in the optimization, until the first switching instant that is scheduled beyond the prediction horizon. In branch 1, for example, this switching instant is given by $t^*_{1(n_1+1)}$.

The constraints (15b)–(15d) are linear and the objective function (15a) is quadratic in the optimization variable. This implies that the optimization problem (15) underlying MP^{3}C is a quadratic program (QP), for which highly efficient solvers are readily available. For a detailed discussion on these and some implementation aspects of MP^{3}C on FPGAs, the interested reader is referred to [21].

We design a model predictive controller (MPC) based on the receding horizon control principle. The controller solves the optimization problem (15) at each sampling instant kT_s and computes the number of MMC modules $u_j \in \{-M, ..., 0, ..., M\}$ to be inserted into each branch $j \in \{1, 2, 3\}$ within the current sampling interval. At the next sampling instant, a new flux reference and a new flux estimate are obtained, and new nominal switching instants and corresponding switching transitions are read in. The optimization procedure is repeated with the new data over a shifted (or receding) prediction horizon.

D. Cell Selection

Each branch uses a dedicated cell selection algorithm that translates the branch switch positions $u_j \in \{-M, \ldots, 0, \ldots, M\}$ into module switch positions $u_{jk} \in \{-1, 0, 1\}$, where $j \in \{1, 2, 3\}$ and $k \in \{1, \ldots, M\}$. The cell selection algorithms exploit the redundancy of the modules in the branches to balance the capacitor voltages of the modules within their branch.

Adopting the sorting algorithm proposed in [3], the modules are sorted according to their capacitor voltages. If current flows into (out of) the branch, the module with the lowest (highest) voltage is inserted. In contrast, the module with the lowest (highest) voltage is removed, when the current flows out of (into) the branch.

VI. Performance Evaluation

Consider the STATCOM in Fig. 1 with $M = 9$ modules per branch. The rated converter voltage is $10.3\,\text{kV}$ and the rated

(a) Active power P (pu) and reactive power Q (pu)

(b) Converter currents $i_{\text{sc,abc}}$ (pu)

(c) Branch voltages v_{123} (pu)

(d) Capacitor voltages v_{c1k} (pu) of the 9 modules in branch 1
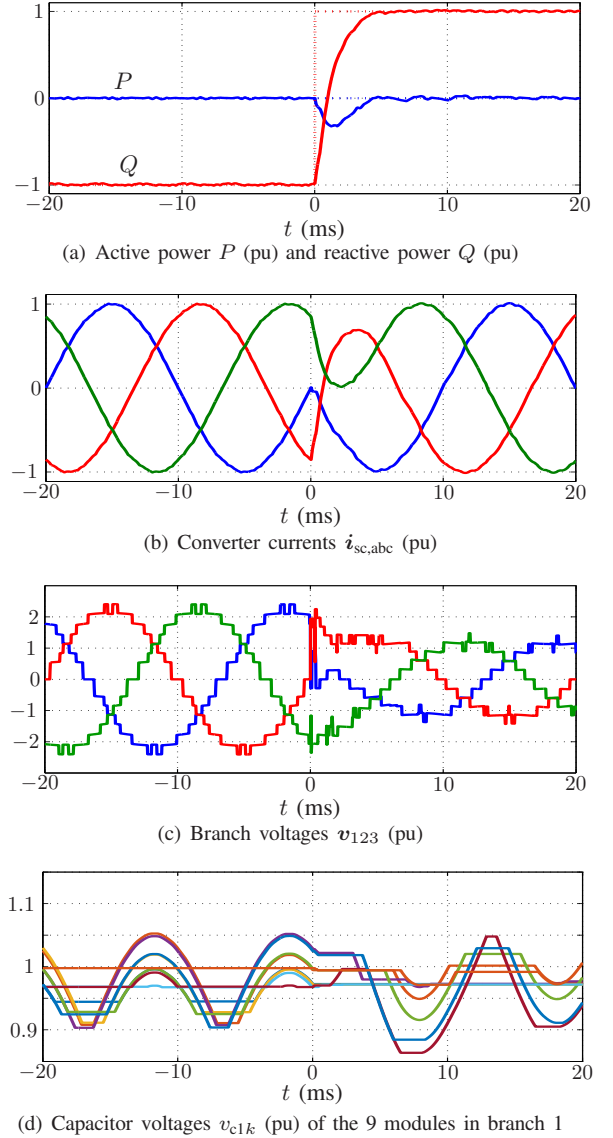
Fig. 7: Reactive power reference step from -1 to $1\,\text{pu}$ at time $t = 0$. The power references are shown as dotted lines

current is in the kiloampere range. A per unit (pu) system is established based on the peak values of the rated phase voltage and current. The inductors are $L_{\text{br}} = L_{\text{sc}} = L_{\text{g}} = 0.1\,\text{pu}$ and the resistors are $R_{\text{br}} = R_{\text{sc}} = R_{\text{g}} = 0.005\,\text{pu}$.

The sampling interval of the controller is $25\mu s$ and the grid frequency is $50\,\text{Hz}$. Unless otherwise stated, MP^{3}C uses an OPP with pulse number $d = 9$, similar to the one shown in Fig. 3. This implies a switching frequency per semiconductor device of $50\,\text{Hz}$.

The switching (power) losses are the sum of the switching energy losses in all three branches over the fundamental period divided by the length in time of the fundamental period. We assume constant capacitor voltages and equal switching losses for all switching events. The switching energy losses are then proportional to the current magnitude when switching. This allows us to state the following measure for the switching

(power) losses:

$$P_{\text{sw}} \sim f_1 \sum_{j=1}^{3} \sum_{\ell=1}^{N_j} |i_j(t_{j,\ell})|, \tag{16}$$

where f_1 denotes the fundamental frequency, and N_j is the number of switching events within a fundamental period in branch j, with $j \in \{1, 2, 3\}$. Recall that $i_j(\cdot)$ is the instantaneous current in the jth branch, and $t_{j,\ell}$ is the time instant of the ℓth switching event in that branch.

A. Steady-State Operation

Consider steady-state operation at the nominal reactive power $Q = 1$ pu, which is injected into the grid. The harmonic amplitude spectra of the converter currents are depicted in Fig. 6. All harmonics including inter-harmonics are grouped with the nearest integer harmonic by computing the rms value of their amplitudes. The amplitude of the resulting harmonic is then normalized using the short-circuit current. The limits imposed by the grid code [2] on the amplitudes of the current harmonics at the PCC are also shown.

Three different control scenarios are considered hereafter. Fig. 6(a) depicts the current spectra for asynchronous carrier-based PWM (CB-PWM) operating at a switching frequency of 150 Hz per semiconductor device. We use this standard modulation method to provide a baseline in terms of switching losses and harmonic performance. The first harmonic to violate the grid code is the 16th.

The harmonic current spectrum in Fig. 6(b) results from the proposed MP³C method operating with an OPP with pulse number $d = 9$. The device switching frequency is approximately 50 Hz, and the switching losses are reduced by 60% when compared to CB-PWM. Lower switching losses increase the system efficiency, allow for a cheaper cooling system, and extend the lifetime of the semiconductor switches. In addition, the harmonic spectrum is slightly improved with respect to CB-PWM, with the first violation of the grid code constraints occurring at the 25th harmonic. Compared to CB-PWM, which operates at three times the switching frequency, significantly fewer (8 instead of 24) grid code violations occur, see Figs. 6(b) and 6(a).

Alternatively, MP³C may use the 150 Hz device switching frequency of CB-PWM; the resulting switching losses are very similar to those of CB-PWM. The harmonic spectrum is, however, superior to that of CB-PWM, as shown in Fig. 6(c). The grid codes are met up to the 63th harmonic, whereas for CB-PWM, the first violation occurs already at the 16th harmonic. We conclude that MP³C enables a significant reduction of the size of an output filter. Note that for CB-PWM to achieve a similar harmonic performance to that of MP³C operating at 150 Hz, a switching frequency of 300 Hz would be required.

It is interesting to notice that the harmonic spectra are qualitatively different between the two control methods; MP³C produces little even and inter-harmonics, which are penalized more heavily by the grid code. The odd harmonics at low frequencies meet the grid code, but they are not fully eliminated. This shaping of the harmonic spectrum extends the
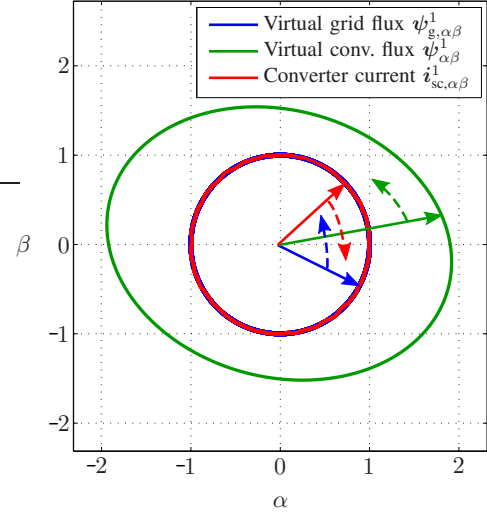
Fig. 8: Injection of a negative-sequence current: virtual fluxes and converter current trajectories in stationary orthogonal coordinates

frequency range for which the grid code can be met without the installation of an output filter.

B. Reactive Power Reference Step

The dynamic response to a reactive power reference step is simulated next. An extreme transient from nominal inductive power $Q = -1$ pu to nominal capacitive power $Q = 1$ pu is considered. The active and reactive power are shown in Fig. 7(a). The latter exhibits a very fast response, with the power transient lasting for less then 5 ms, i.e.less than a quarter of the fundamental period. During this transient, the phase of the current is shifted by 180°, as can be seen in Fig. 7(b).

The branch voltages are depicted in Fig. 7(c). Before and after the transient, the characteristic switching pattern of the OPP is clearly recognizable. During the transient, however, MP³C strongly modifies the pulse pattern in order to accomplish a fast transient. To facilitate this, pulse insertion as described in [22] is used for the MP³C algorithm. The capacitor voltages of the individual modules are disturbed by the transient. The dc components of the capacitor voltages are offset by at most 25% of their peak-to-peak voltage ripple. The cell selection algorithm quickly removes any dc offset and restores the equilibrium within two fundamental periods. Fig. 7(d) shows the nine capacitor voltages of the first MMC branch.

C. Negative-Sequence Current Injection

Consider the balanced grid voltage

$$\boldsymbol{v}_{\text{g,abc}} = \begin{bmatrix} \cos(\omega_1 t) \\ \cos(\omega_1 t - \frac{2\pi}{3}) \\ \cos(\omega_1 t + \frac{2\pi}{3}) \end{bmatrix} \text{ or } \boldsymbol{v}_{\text{g},\alpha\beta\gamma} = \begin{bmatrix} \cos(\omega_1 t) \\ \sin(\omega_1 t) \\ 0 \end{bmatrix}$$

and unbalanced operation. The STATCOM is required to inject a negative-sequence converter current with the reference

$$\boldsymbol{i}_{\text{sc,abc}}^{1*} = \begin{bmatrix} \cos(\omega_1 t) \\ \cos(\omega_1 t + \frac{2\pi}{3}) \\ \cos(\omega_1 t - \frac{2\pi}{3}) \end{bmatrix} \text{ or } \boldsymbol{i}_{\text{sc},\alpha\beta\gamma}^{1*} = \begin{bmatrix} \cos(\omega_1 t) \\ -\sin(\omega_1 t) \\ 0 \end{bmatrix}$$

into the grid to compensate for a corresponding load current. To accomplish this, the fundamental component of the virtual converter flux is required to be

$$\boldsymbol{\psi}_{\alpha\beta}^{1*} = \sqrt{3}\boldsymbol{D}^T(L_{\text{eq}}\boldsymbol{i}_{\text{sc},\alpha\beta}^{1*} + \boldsymbol{\psi}_{\text{PCC},\alpha\beta}^1)$$

in accordance with (13a).

The trajectories of the virtual grid flux, virtual converter flux and the injected converter current are shown in Fig. 8 in stationary orthogonal coordinates. Note that the (negative-sequence) current vector rotates clockwise, whereas the virtual grid and converter flux vectors rotate in an anti-clockwise direction. The latter forms an ellipsoidal trajectory.

The corresponding simulation results are summarized in Fig. 9. Figs. 9(a) and 9(b) show that the three-phase grid voltage and the injected converter current have the expected phase shifts; phases a, b and c of the grid voltage are aligned with phases a, c and b of the converter current. Fig. 9(c) shows the three branch voltages, which have, as expected, different amplitudes and use different OPPs (with different fundamental components and non-120° phase shifts between them). Accordingly, the currents in the three branches differ significantly, with branch 2 exhibiting a particularly low current amplitude, as can be seen in Fig. 9(d).

This implies a significant circulating current in the converter, as shown in Fig. 9(e). This circulating current arises irrespectively of the chosen control method; rather, it is dictated by the operating point, particularly the imbalances in the converter currents. The reference for the circulating current, which is shown as the dashed line, is determined from the flux reference ψ_γ^* according to (13b). MP^{3}C tracks the γ-flux reference well, albeit with a small phase lag.

D. Harmonic Current Injection

Last, the system response to the asymmetrical harmonic current reference

$$\boldsymbol{i}_{\text{sc,abc}}^{\text{h}*} = 0.04 \begin{bmatrix} \sin(3\omega_1 t) + \sin(13\omega_1 t) \\ -\sin(3\omega_1 t) - \sin(13\omega_1 t) \\ 0 \end{bmatrix} \qquad (17)$$

is investigated. Operation is at a device switching frequency of 150 Hz. The tracking of the converter current in the time domain is shown in Fig. 10(a), whereas Fig. 10(b) depicts the harmonic spectrum of the three-phase output current. The tracking performance is good, particularly in light of the low device switching frequency of 150 Hz. The inserted 4th and 13th harmonics can be clearly identified in the harmonic spectrum and have a magnitude of approximately 0.04 pu, as required by the reference (17).

An OPP, which was computed offline for steady-state operation, is not suitable for harmonic current injection. Instead, MP^{3}C achieves harmonic current injection by aggressively correcting the switching instants of the OPP and by inserting additional pulses as described in [22]. More specifically, an OPP with a device switching frequency of 50 Hz is used, and the pulse insertion mechanism increases the switching frequency to 150 Hz. For this kind of operating regime, pulse

(a) Grid voltage $\boldsymbol{v}_{\text{g,abc}}$ (pu)

(b) Converter current $\boldsymbol{i}_{\text{sc,abc}}$ (pu)

(c) Branch voltage $\boldsymbol{v}_{123}$ (pu)

(d) Branch current $\boldsymbol{i}_{123}$ (pu)

(e) Circulating current i_{circ} (pu)
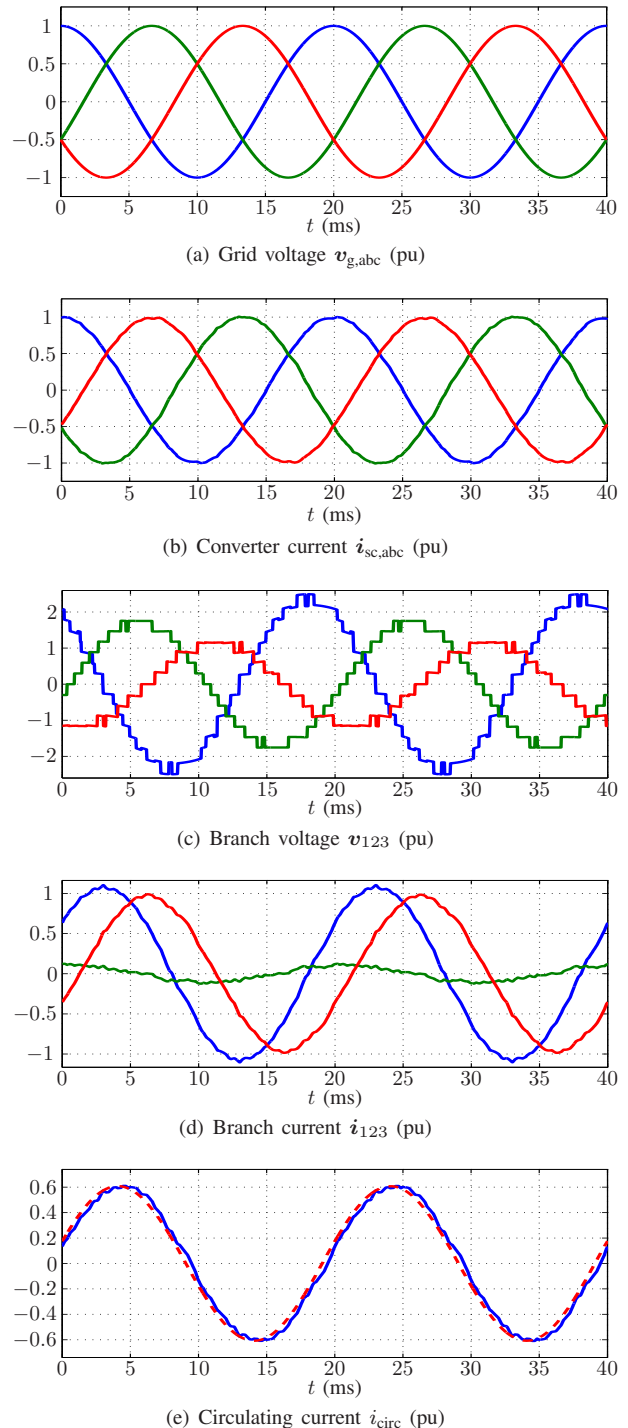
Fig. 9: Injection of a negative-sequence current

insertion achieves a better tracking performance than when using OPPs with a higher pulse number. This is due to the fact that MP^{3}C inserts pulses at time instants in the fundamental cycle where they best improve the tracking of the harmonic current reference.

Note that a switching frequency of 150 Hz implies 27 switching transition per quarter of the fundamental period. For the 13th harmonic component, only $27/13 = 2.08$ switching

(a) Current references (dashed lines) and converter currents (solid lines)

(b) Harmonic amplitude spectrum
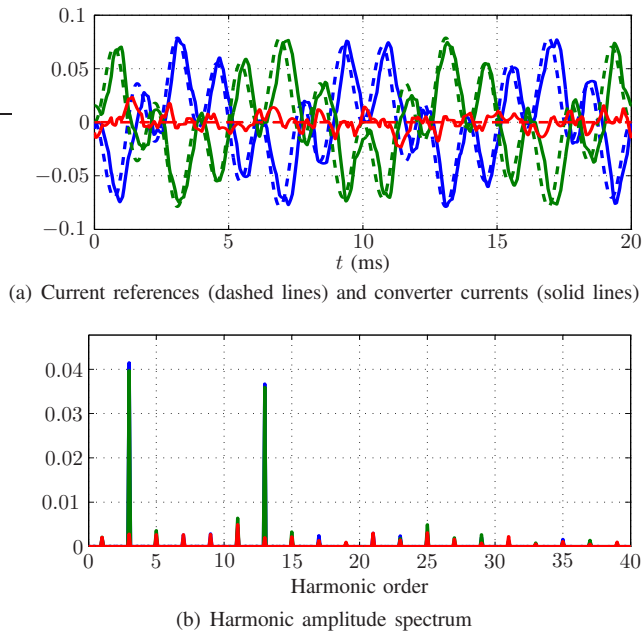
Fig. 10: Injection of a harmonic converter current $\boldsymbol{i}_{\text{sc,abc}}^{\text{h}}$ (pu). The colours blue, green and red refer to phase a, b and c, respectively

transitions are available per quarter-period. MP³C performs remarkably well at this low ratio between switching frequency and harmonic current frequency.

VII. DISCUSSION

During nominal operation, i.e. reactive power injection or absorption, the applied switching patterns are very similar to those of the nominal OPPs, thus achieving converter current waveforms with optimal harmonic spectra. When varying the fundamental component (i.e. the modulation index), the OPPs may exhibit discontinuities in their switching angles; the fast online control mechanism of MP³C allows for seamless transitions between OPPs around angular discontinuities. Specifically, deviations in the converter currents are avoided.

Triplen harmonics are common-mode harmonics and thus cancel out in the converter currents. In the branch currents, however, they drive triplen circulating current harmonics. Indeed, control of the circulating current is achieved by controlling the common-mode converter flux, which is the integral of the common-mode voltage. Therefore, it is advisable to use OPPs, whose triplen harmonics have reduced amplitudes.

During unbalanced operation, such as when injecting negative-sequence currents, the trajectory of the virtual converter flux is non-circular. To achieve this operation, different OPPs (with different fundamental components and with non-120° phase-shifts between them) are used in the three MMC branches. As a consequence, the triplen harmonics are no longer pure common-mode harmonics, but can have a significant differential-mode component. This further justifies the computation of OPPs with reduced triplen harmonics.

Classic OPP-based control systems use linear PI control loops, e.g. in a voltage-oriented controller setting, that manip-

ulate fundamental voltage references (or modulation indices), which are fed to a separate modulator. During a transient, the PI current controllers change the fundamental voltage references and thus use different pulse patterns. Because of that, the use of pulse patterns with continuous switching angles is mandatory; this can be achieved by adopting selective harmonic elimination (SHE) as a technique to compute such patterns [14].

The proposed MPC scheme, however, addresses the current (or virtual flux) control problem and the PWM in one computational stage. Dynamic control is *not* accomplished by switching to a new OPP, but rather by modifying the switching instants of the OPP through MP³C. The virtual converter flux trajectory based on the OPP is optimal in the sense that it encodes the optimal harmonic current spectrum that meets the grid codes. By tracking this flux trajectory, MP³C ensures that during steady-state operation the optimal harmonic spectrum is obtained despite variations in the capacitor voltages of the modules, system delays and small disturbances. OPPs with a different fundamental component are only selected when the steady-state operating point changes, but not to reject disturbances or to achieve transients.

VIII. CONCLUSIONS

An OPP-based control system for delta-connected MMC STATCOMs was proposed in this paper. By computing OPPs that meet the relevant grid codes, the MP³C scheme provides an excellent harmonic current spectrum while operating at device switching frequencies at or below 150 Hz. Compared to classic control and modulation methods such as carrier-based PWM, the switching losses can be either reduced for a similar current spectrum, or the current spectrum can be significantly improved for similar switching losses.

This increases the system efficiency and reduces the size of the output filter, lowering the cost of the overall converter system. Thanks to the fast MPC-based control methodology modifying the OPPs, the proposed control scheme is able to address the control objectives inherent to STATCOMs, such as very fast responses to transients and power steps, and the compensation for negative-sequence and harmonic currents at the PCC.

APPENDIX A

The equation systems (3) and (5) are derived in this appendix. Left-multiplying each equation in (2) with the Clarke transformation matrix $\boldsymbol{K}$ leads to

$$\boldsymbol{v}_{\alpha\beta\gamma} = L_{\text{br}}\frac{\mathrm{d}\boldsymbol{i}_{\alpha\beta\gamma}}{\mathrm{d}t} + R_{\text{br}}\boldsymbol{i}_{\alpha\beta\gamma} + \boldsymbol{D}_1'\boldsymbol{v}_{\text{g},\alpha\beta\gamma} + \tag{18a}$$

$$+ \boldsymbol{D}_1'\left(L_{\text{sc}}\frac{\mathrm{d}\boldsymbol{i}_{\text{sc},\alpha\beta\gamma}}{\mathrm{d}t} + R_{\text{sc}}\boldsymbol{i}_{\text{sc},\alpha\beta\gamma} + L_{\text{g}}\frac{\mathrm{d}\boldsymbol{i}_{\text{g},\alpha\beta\gamma}}{\mathrm{d}t} + R_{\text{g}}\boldsymbol{i}_{\text{g},\alpha\beta\gamma}\right),$$

$$\boldsymbol{i}_{\text{sc},\alpha\beta\gamma} = \boldsymbol{D}_2'\boldsymbol{i}_{\alpha\beta\gamma}, \tag{18b}$$

$$\boldsymbol{i}_{\text{g},\alpha\beta\gamma} = \boldsymbol{i}_{\text{sc},\alpha\beta\gamma} - \boldsymbol{i}_{\text{l},\alpha\beta\gamma}, \tag{18c}$$

with

$$\boldsymbol{D}_1' = \boldsymbol{K}\boldsymbol{D}_1\boldsymbol{K}^{-1} = \begin{bmatrix} \sqrt{3}\boldsymbol{D}^T & \boldsymbol{0}_{2\times1} \\ \boldsymbol{0}_{1\times2} & 0 \end{bmatrix}$$

and

$$D_2' = K D_2 K^{-1} = \begin{bmatrix} \sqrt{3}D & \mathbf{0}_{2\times1} \\ \mathbf{0}_{1\times2} & 0 \end{bmatrix}.$$

D was defined in (4), $\mathbf{0}_{1\times2}$ is a 1×2 zero vector, and $\mathbf{0}_{2\times1}$ is a 2×1 zero vector.

Owing to the block diagonal characteristic of D_1' and D_2', (18) can be separated into differential-mode and common-mode equations. The differential-mode equations directly follow to

$$v_{\alpha\beta} = L_{\text{br}}\frac{\mathrm{d}i_{\alpha\beta}}{\mathrm{d}t} + R_{\text{br}}i_{\alpha\beta} + \sqrt{3}D^T v_{\text{g},\alpha\beta}+ \quad (19\text{a})$$

$$+ \sqrt{3}D^T \left(L_{\text{sc}}\frac{\mathrm{d}i_{\text{sc},\alpha\beta}}{\mathrm{d}t} + R_{\text{sc}}i_{\text{sc},\alpha\beta} + L_{\text{g}}\frac{\mathrm{d}i_{\text{g},\alpha\beta}}{\mathrm{d}t} + R_{\text{g}}i_{\text{g},\alpha\beta} \right),$$

$$i_{\text{sc},\alpha\beta} = \sqrt{3}D i_{\alpha\beta}, \quad (19\text{b})$$

$$i_{\text{g},\alpha\beta} = i_{\text{sc},\alpha\beta} - i_{\text{l},\alpha\beta}, \quad (19\text{c})$$

which can be further simplified. We left-multiply (19a) with $1/\sqrt{3}D$, exploit the fact that $D^{-1} = D^T$, and insert (19b) into the equation. This simplifies (19a) to

$$\frac{1}{\sqrt{3}}D v_{\alpha\beta} = v_{\text{g},\alpha\beta} + (L_{\text{sc}} + \frac{1}{3}L_{\text{br}})\frac{\mathrm{d}i_{\text{sc},\alpha\beta}}{\mathrm{d}t}+$$

$$+ (R_{\text{sc}} + \frac{1}{3}R_{\text{br}})i_{\text{sc},\alpha\beta} + L_{\text{g}}\frac{\mathrm{d}i_{\text{g},\alpha\beta}}{\mathrm{d}t} + R_{\text{g}}i_{\text{g},\alpha\beta}.$$

The common-mode equations directly follow from (18) to

$$v_\gamma = L_{\text{br}}\frac{\mathrm{d}i_\gamma}{\mathrm{d}t} + R_{\text{br}}i_\gamma, \quad (20\text{a})$$

$$i_{\text{sc},\gamma} = 0, \quad (20\text{b})$$

$$i_{\text{g},\gamma} = 0. \quad (20\text{c})$$

APPENDIX B

Which fundamental-component converter voltage $v_{\alpha\beta}^1$ corresponds to the fundamental-component virtual converter flux vector $\psi_{\alpha\beta}^1$? During steady-state operation, the latter can be written in terms of the flux angle $\theta = \omega_1 t$ and the flux magnitude Ψ as

$$\psi_{\alpha\beta}^1 = \Psi \begin{bmatrix} \cos(\theta) \\ \sin(\theta) \end{bmatrix}. \quad (21)$$

The converter voltage is the derivative of the virtual converter flux, see also (9a). This allows us to write

$$v_{\alpha\beta}^1 = \frac{\mathrm{d}}{\mathrm{d}t}\psi_{\alpha\beta}^1 = \Psi\,\omega_1 \begin{bmatrix} -\sin(\theta) \\ \cos(\theta) \end{bmatrix} = \omega_1 \begin{bmatrix} 0 & -1 \\ 1 & 0 \end{bmatrix} \psi_{\alpha\beta}^1. \quad (22)$$

The converter voltage is thus equal to the virtual converter flux rotated forward by 90 degrees and scaled by the angular grid frequency.

REFERENCES

[1] B. Singh, R. S. amd A. Chandra, and K. Al-Haddad, "Static synchronous compensators (STATCOM): A review," *IET Power Electron.*, vol. 2, pp. 297–324, Jul. 2009.

[2] Bundesverband der Energie- und Wasserwirtschaft e.V. (BDEW), "Erzeugungsanlagen am Mittelspannungsnetz. Richtlinie für Anschluss und Parallelbetrieb von Erzeugungsanlagen am Mittelspannungsnetz," Jun. 2008.

[3] A. Lesnicar and R. Marquardt, "An innovative modular multilevel converter topology suitable for a wide power range," in *Proc. IEEE Power Tech. Conf.*, (Bologna, Italy), Jun. 2003.

[4] H. M. Pirouz and M. T. Bina, "Modular multilevel converter based STATCOM topology suitable for medium-voltage unbalanced systems," *J. of Power Electron.*, vol. 10, pp. 572–578, Sep. 2010.

[5] S. Debnath, J. Qin, B. Bahrani, M. Saeedifard, and P. Barbosa, "Operation, control, and applications of the modular multilevel converter: A review," *IEEE Trans. Power Electron.*, vol. 30, pp. 37–53, Jan. 2015.

[6] M. A. Pérez, S. Bernet, J. Rodríguez, S. Kouro, and R. Lizana, "Circuit topologies, modeling, control schemes, and applications of modular multilevel converters," *IEEE Trans. Power Electron.*, vol. 30, pp. 4–17, Jan. 2015.

[7] G. S. Buja, "Optimum output waveforms in PWM inverters," *IEEE Trans. Ind. Appl.*, vol. 16, pp. 830–836, Nov./Dec. 1980.

[8] I. Colak, E. Kabalci, and R. Bayindir, "Review of multilevel voltage source inverter topologies and control schemes," *Energy Convers. and Mgmt.*, vol. 52, pp. 1114–1128, Feb. 2011.

[9] V. Spudić and T. Geyer, "Fast control of a modular multilevel converter STATCOM using optimized pulse patterns," in *Proc. IEEE Energy Convers. Congr. Expo.*, (Cincinnati, OH, USA), Oct. 2017.

[10] T. Geyer, N. Oikonomou, G. Papafotiou, and F. Kieferndorf, "Model predictive pulse pattern control," *IEEE Trans. Ind. Appl.*, vol. 48, pp. 663–676, Mar./Apr. 2012.

[11] M. Vasiladiotis, A. Christe, and T. Geyer, "Model predictive pulse pattern control for modular multilevel converters," *IEEE Trans. Ind. Electron.*, vol. 66, pp. 2423–2431, 3 2019.

[12] M. Vasiladiotis, A. Christe, T. Geyer, and A. Faulstich, "Decoupled modulation concept for three-to-single-phase direct AC/AC modular multilevel converters for railway interties," in *Proc. Eur. Power Electron. Conf.*, (Warsaw, Poland), Sep. 2017.

[13] H. S. Patel and R. G. Hoft, "Generalized techniques of harmonic elimination and voltage control in thyristor inverters: Part I–Harmonic elimination," *IEEE Trans. Ind. Appl.*, vol. IA-9, pp. 310–317, May/Jun. 1973.

[14] J. N. Chiasson, L. M. Tolbert, K. J. McKenzie, and Z. Du, "Elimination of harmonics in a multilevel converter using the theory of symmetric polynomials and resultants," *IEEE Trans. Contr. Syst. Technol.*, vol. 13, pp. 216–223, Mar. 2005.

[15] H. Akagi, "New trends in medium-voltage power converters and motor drives," in *Proc. IEEE Int. Symp. Ind. Electron.*, (Gdansk, Poland), Jun. 2011.

[16] J. I. Y. Ota, Y. Shibano, N. Niimura, and H. Akagi, "A phase-shifted-PWM D-STATCOM using a modular multilevel cascade converter (SSBC)—Part I: Modeling, analysis, and design of current control," *IEEE Trans. Ind. Appl.*, vol. 51, pp. 279–288, Jan./Feb. 2015.

[17] M. Rashid, *Power electronics handbook: devices, circuits and applications.* Acad. Press, 2nd ed., 2006.

[18] T. Geyer, *Model predictive control of high power converters and industrial drives.* London, UK: Wiley, Oct. 2016.

[19] A. Edpuganti and A. K. Rathore, "A survey of low switching frequency modulation techniques for medium-voltage multilevel converters," *IEEE Trans. Ind. Appl.*, vol. 51, pp. 4212–4228, Sep./Oct. 2015.

[20] R. Picas, J. Pou, S. Ceballos, J. Zaragoza, G. Konstantinou, and V. Angelidis, "Optimal injection of harmonics in circulating currents of modular multilevel converters for capacitor voltage ripple minimization," in *ECCE Asia Downunder*, pp. 318–324, Jun. 2013.

[21] S. Richter, T. Geyer, and M. Morari, "Resource-efficient gradient methods for model predictive pulse pattern control on an FPGA," *IEEE Trans. Contr. Syst. Technol.*, vol. 25, pp. 828–841, May 2017.

[22] T. Geyer and N. Oikonomou, "Model predictive pulse pattern control with very fast transient responses," in *Proc. IEEE Energy Convers. Congr. Expo.*, (Pittsburgh, PA, USA), Sep. 2014.